Nanopore Sensors for Enhanced Detection of Nanoparticles

Samuel Confederat[1,2], Seungheon Lee[3], Der Wang[4], Dimitrios Soulias[1,2,5], Fabio Marcuccio[1,2,6], Timotheus I. Peace[1,2,7], Martin Andrew Edwards[8], Pietro Strobbia[4], Devleena Samanta[3], Christoph Wälti[1,2], Paolo Actis[1,2]

[1] School of Electronic and Electrical Engineering and Pollard Institute, University of Leeds, Leeds LS2 9JT, UK

[2] Bragg Centre for Materials Research, University of Leeds, LS2 9JT, UK

[3] Department of Chemistry, The University of Texas at Austin, Austin, TX 78712 USA

[4] Department of Chemistry, University of Cincinnati, Cincinnati, Ohio 45221, USA

[5] Department of Chemistry, University of Oxford, Oxford OX1 3QZ, UK

[6] Faculty of Medicine, Imperial College London, London SW7 2AZ, UK

[7] School of Molecular and Cellular Biology and Astbury Centre for Structural Molecular Biology, University of Leeds, Leeds LS2 9JT, UK

[8] Department of Chemistry and Biochemistry, University of Arkansas, Fayetteville, AK, 72701, USA

KEYWORDS: nanopores, nanoparticle mixtures, functionalized proteins, single-molecule analysis, nanoparticle characterization

* Corresponding authors; maedw@uark.edu; strobbpo@ucmail.uc.edu; dsamanta@utexas.edu; c.walti@leeds.ac.uk; p.actis@leeds.ac.uk

ABSTRACT

Nanopore sensing is a technique based on the Coulter principle to analyze and characterize biological molecules with single molecule resolution. However, its use in nanoparticle characterization has been constrained by the need to tailor the nanopore aperture size based on the size of the analyte, precluding the analysis of heterogenous samples. Additionally, nanopore sensors often require the use of high salt concentrations to improve the signal-to-noise ratio, which further limits their ability to study a wide range of nanoparticles that are unstable at high ionic strength.

Here we show the development of nanopore sensors enhanced by a polymer electrolyte system, enabling the analysis of heterogenous nanoparticle mixtures at low ionic strength. We present a finite element model to explain the anomalous conductive pulse signals observed and compare these results with extensive experiments. Furthermore, we demonstrate the wide applicability of the method by characterizing metallic nanospheres of different sizes, plasmonic nanostars with various degrees of branching, and protein-based spherical nucleic acids with different oligonucleotide loadings.

Our system complements existing nanomaterials characterization techniques and enables the electrical and real-time optimization workflow for engineering a wide range of nanomaterials.

INTRODUCTION

Over the past few decades, the use of nanoparticles has played a major role in the advancement of medicine, optics, and electronics (1-3). Therefore, the ability to characterize nanoparticles in a high-throughput manner is of utmost importance. However, characterizing nanoparticles in their native state, specifically in heterogenous mixtures, presents many challenges (4). Dynamic light scattering (DLS) or UV-Vis spectroscopy are ensemble-averaging techniques and, therefore, fall short in fully characterizing heterogenous nanoparticle mixtures (5). Methods such as transmission electron microscopy (TEM) provide high-resolution characterization of individual nanoparticles but suffer from low throughput, and require careful sample preparation (6).

Nanopore sensing is a powerful label-free electrical technique that uses the Coulter principle to analyze and characterize biological molecules with single molecule resolution, but it has an untapped potential for the analysis of nanoparticles (7). This is because current nanopore measurements require the size of the pore to match the size of the analyte, limiting the investigation to homogenous mixtures (8-10). Furthermore, nanopore measurements require high-ionic-concentration electrolytes which precludes the analysis of nanoparticles systems that are unstable at high ionic strength (11,12). Tunable resistive pulse sensing (TRPS) is a nanopore technique that has found some applications in nanoparticle characterization, but it is limited to nanoparticles larger than 100 nm in size (13,14). Furthermore, the TRPS signals deviate from linearity when the size of the nanoparticle approaches the diameter of the pore aperture, limiting its analytical capabilities.

Here, we present polymer-electrolyte enhanced nanopore sensing which offers a fundamentally new approach for single-nanoparticle analysis. The polymer electrolyte

environment generates a large signal enhancement eliminating the need for a nanopore that matches the size of the nanoparticle and therefore allowing the high throughput analysis of heterogenous nanoparticle mixtures. Furthermore, combining experimental findings and finite-element modelling (FEM), we show that the ion current signatures obtained using a polymer-electrolyte enhanced nanopore system can enable the characterization of nanoparticles at low ionic strength (10 mM) thus enabling the characterization of anisotropic gold nanostars (AuNS) with varying degrees of branching. We then demonstrate the detection and analysis of a class of functional soft nanoparticles, protein spherical nucleic acids (ProSNAs) with distinct oligonucleotides shells. The single-nanoparticle-analysis approach described herein will complement the toolbox of existing nanomaterials characterization techniques.

RESULTS AND DISCUSSION

A polymer electrolyte nanopore (15) system enables the detection of heterogenous nanoparticle mixtures with a fixed nanopore size. We fabricated glass nanopores with a diameter of 60 nm and probed the translocation of 20 nm gold nanoparticles (AuNPs) samples (Figure 1) under an applied voltage of -500 mV. The nanopore setup consisted of glass nanopore immersed in an electrolyte (KCl) solution where the application of potential inside the glass pore drives the translocation of the analyte in the external bath using a pair of Ag/AgCl electrodes. As shown in Figure 1A, no translocation events were observed for the 20 nm AuNPs using standard electrolyte buffer conditions (*i.e.* 50mM KCl solution). However, the addition of 50% w/v PEG (polymer electrolyte) to the outer bath resulted in conductive translocation events well-resolved from the ion current baseline (Figure 1B). These events are characterised by a specific peak amplitude (ΔI_c) and dwell time (Figure 1B

inset), where each peak is generated by one nanoparticle translocating from inside the pore to the outer bath. No events were observed under the application of a positive voltage or in absence of nanoparticles in solution (Figure S6). Increasing the magnitude of the applied voltage led to an increase in amplitude of the conductive peak current and a decrease in the dwell time, suggesting that the electrophoretic force plays a major contribution in driving the negatively charged AuNPs through the pore (Figure S7). Similarly, we observed a linear increase in the frequency of the translocation events with increasing voltage and increasing nanoparticle concentrations (Figure S7). Even at a nanoparticle concentration of 6 μg/ml, we were able to record over 300 events per minute and we could record ion current traces for several minutes without any evidence of clogging or drift.

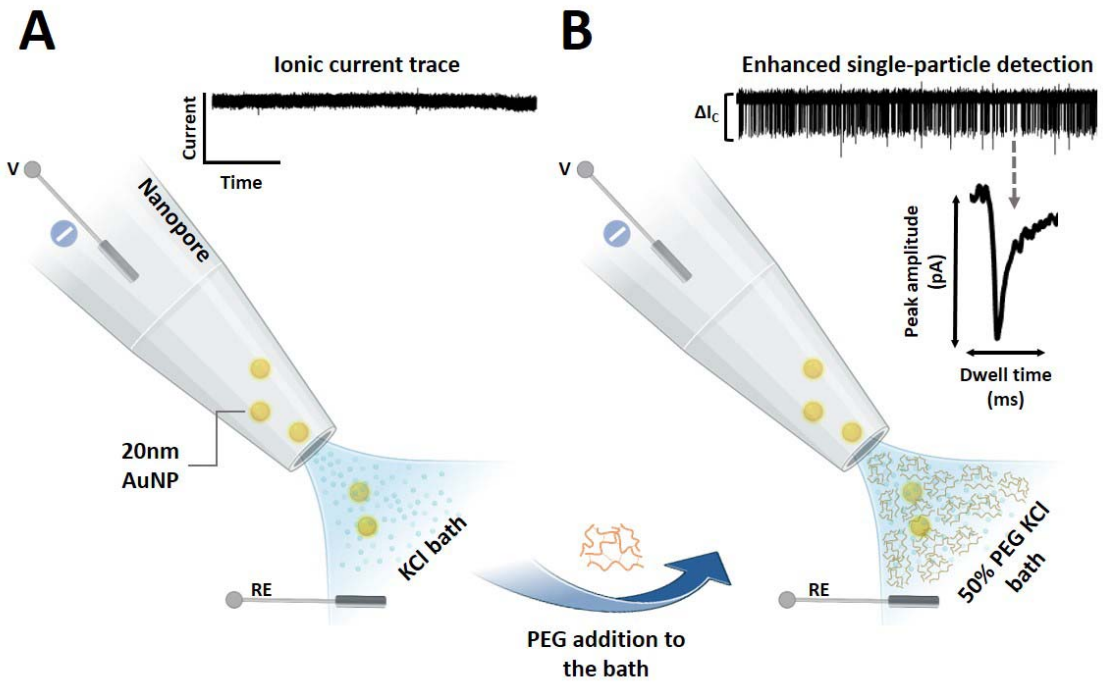

FIGURE 1. Enhanced nanoparticle detection with polymer electrolyte bath **(A)** Schematic depicting 20 nm AuNPs translocating across the nanopore into the outside and the recorded ion current trace at -500 mV for 20 nm AuNPs utilizing a 50 mM KCl external electrolyte bath. No translocation events were observed under these conditions. **(B)** Representative translocation setup depicting the use of 50% (w/v) PEG (polymer electrolyte) in 50 mM KCl in the external electrolyte bath with the corresponding recorded ion current trace at -500 mV, showing conductive translocation events for

20 nm AuNPs. A representative translocation event is shown in the inset with the translocation peak amplitude and dwell time characteristics.

Figure S4 depicts the translocation of a 50 nm and 20 nm AuNP mixture where two distinct peak amplitudes can be observed that also result in distinct populations in the events scatter plots (Figure S4C). The average peak amplitude was 61.1 ± 0.1 pA for the 20 nm AuNPs and 225 ± 1 pA for the 50 nm AuNPs. The large amplitude difference denotes the strong signal enhancement generated by the polymer electrolyte that allowed us to further probe a range of different AuNPs (50, 40, 30, 20, and 10 nm diameter) with a fixed nanopore size (60 nm in diameter) as shown in Figure 2A. The translocation signals were fitted to Gaussian curves which enabled the identification of 5 distinct distributions, one for each nanoparticle set (Figure 2B). Furthermore, we observed that the average conductive peak current increased linearly with the nanoparticle diameter (Figure 2C). To further support the capability of our nanopore approach to discriminate heterogeneous nanoparticles mixtures, in Figure S8 we compared the translocation of individual AuNP solutions with a mixture containing all AuNPs (50, 40, 30, 20, and 10 nm) in one solution. In contrast to previous nanopore strategies employing chemical modifications (16) or arrayed nanopores (17), our nanopore system supports rapid detection of heterogenous nanoparticles and clear discrimination of their size with a fixed nanopore size.

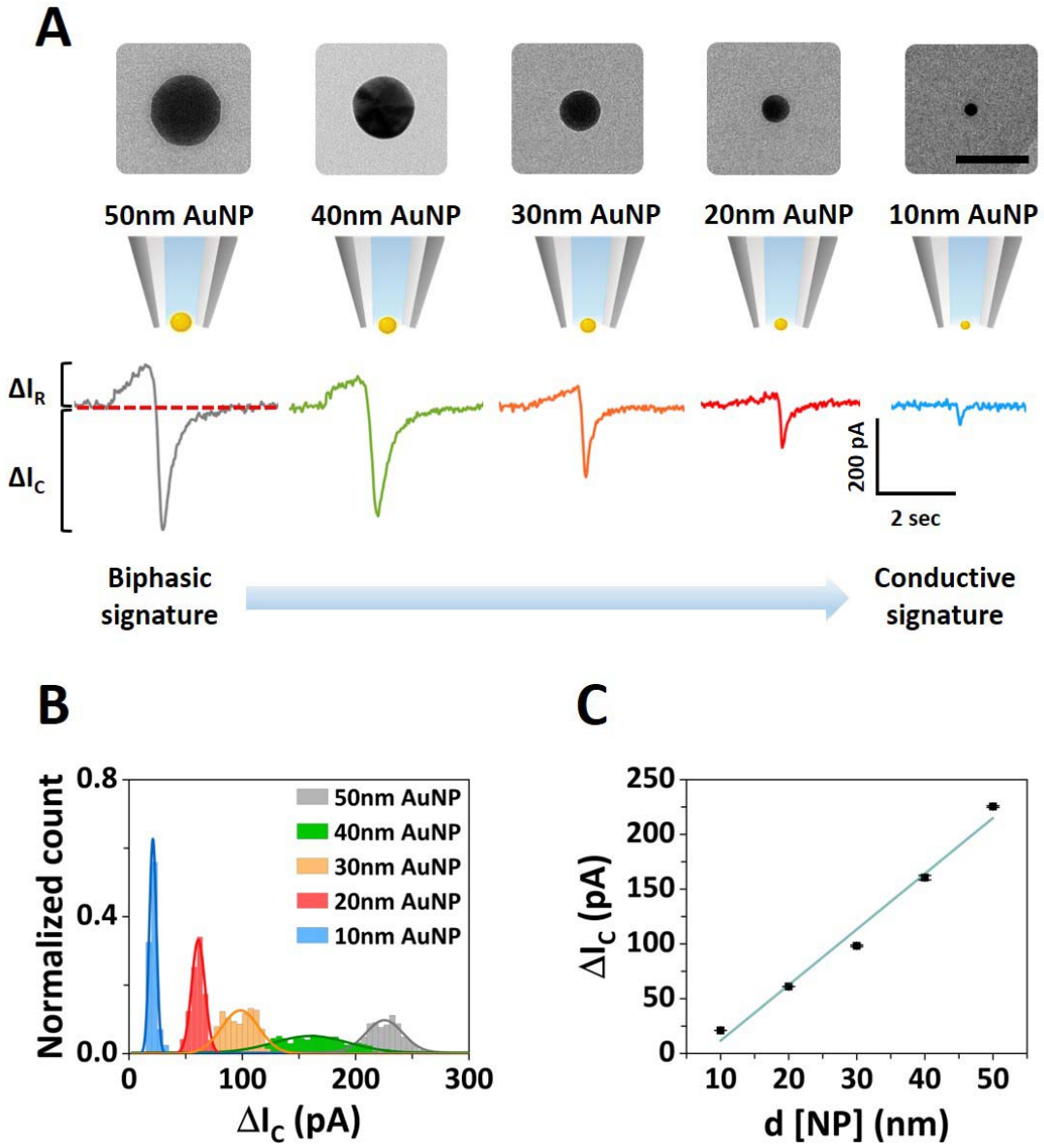

FIGURE 2. Nanopore detection of gold nanoparticle mixtures. **(A)** Top panel: TEM images of the standard AuNPs, left-to-right: 50, 40, 30, 20, and 10 nm diameter (50 nm scale bar). Bottom panel: schematic representation of the AuNP translocating through a 60nm fixed pore size with representative individual translocation peaks for each AuNP, denoting a transition from biphasic to conductive signature when the ratio of nanoparticle to pore size decreases. **(B)** Event histogram of the conductive peak current for the 5 different AuNPs (50, 40, 30, 20, and 10 nm) translocated with a fixed pore size (60 nm). The solid lines represent Gaussian fits to each translocation data set. **(C)** Average conductive peak current as a function of nanoparticle diameter (the blue line represents a linear fit to the data). The error bars represent the standard error of the Gaussian fits displayed in panel B.

Whereas the conductive peak represents the dominant feature investigated in our translocation measurement, we observed a distinct change in the translocation signature when different nanoparticle to pore size ratios were employed. Namely, when the size of the nanoparticle closely matched the size of the pore, an additional resistive peak was observed (Figure S9). This behaviour is evidenced in Figure 2A, where a transition from biphasic (resistive and conductive peak) signal to a conductive signal when the size of the AuNP decreases with respect to the size of the pore (Table S1) or vice versa (Figure S10). Classically, nanoparticle analysis with nanopores leads to resistive (current-decreasing) translocation signals because of the ion flow hindrance by the presence of the nanoparticle within the nanopore sensing region (18). However, several studies have shown the occurrence of conductive peaks. Sensale *et al.* indicated the surface charge of the particle as main factor that influences the characteristics of the translocation signal through a glass nanopores (19). The authors suggested that this phenomenon occurs due to an ion accumulation/depletion associated with the surface charge of the particle translocating through the pore. Similarly, in the studies conducted by Menestrina *et al.* and Chen *et al.,* biphasic signals were reported both experimentally and in simulations when charged particles are translocated in low salt buffer conditions (below 200 mM KCl) (20,21). The authors reported resistive peaks followed by a conductive component and explained the effect considering the charge carried by the analyte that causes a temporary ion enrichment at the aperture when low-salt conditions are used. The phenomenon of the current enhancement can be influenced by several factors, including the electrolyte concentration, nanoparticle to pore size ratio, and the nanoparticle surface charge (22). To investigate the origin of the conductive contribution to the peak in our nanopore system, we developed a finite-element model to estimate the potential resulting current enhancement when a polymer electrolyte (50% PEG) is used in the external solution (23).

We hypothesised that an interface is formed at the nanopore tip between the KCl only and the polymer electrolyte bath, and that this interface is deformed by a model nanoparticle (50 nm) translocating through the pore. This deformation induces an ionic rearrangement within the nanopore producing the single nanoparticle events. Interestingly and counter-intuitively the presence of the nanoparticle in the nanopore sensing area leads to an increase in the ionic concentration due to the deformation of the interface which far outweighs the volume-exclusion-related decrease, thereby overall yielding a temporary

current increase which manifests in a conductive peak. Remarkably, although we simulated the effect of the presence of a nanoparticle at different locations within the nanopore at equilibrium for each position (Figure 3A), we observed an excellent agreement with the experimentally measured resistive and conductive signal (Figures 3B and 3C). We note that we do not have experimental data on the nature of the interface at the nanopore between the inner and the outer bath and therefore assumed it to be a straight line at z = 0 nm. This is clearly an over-simplification and the interface is likely to be more diffuse. Also, our stationary and ergodic model may not capture the full dynamics of the nanoparticle translocation across the interface, but it does capture the underlying process and provides a good phenomenological understanding of the impact of the nanoparticle translocation on the ion current. Using a more sophisticated fully dynamic model would certainly improve the accuracy of the predictions but would unlikely lead to a significant revision of the phenomenological understanding of the system.

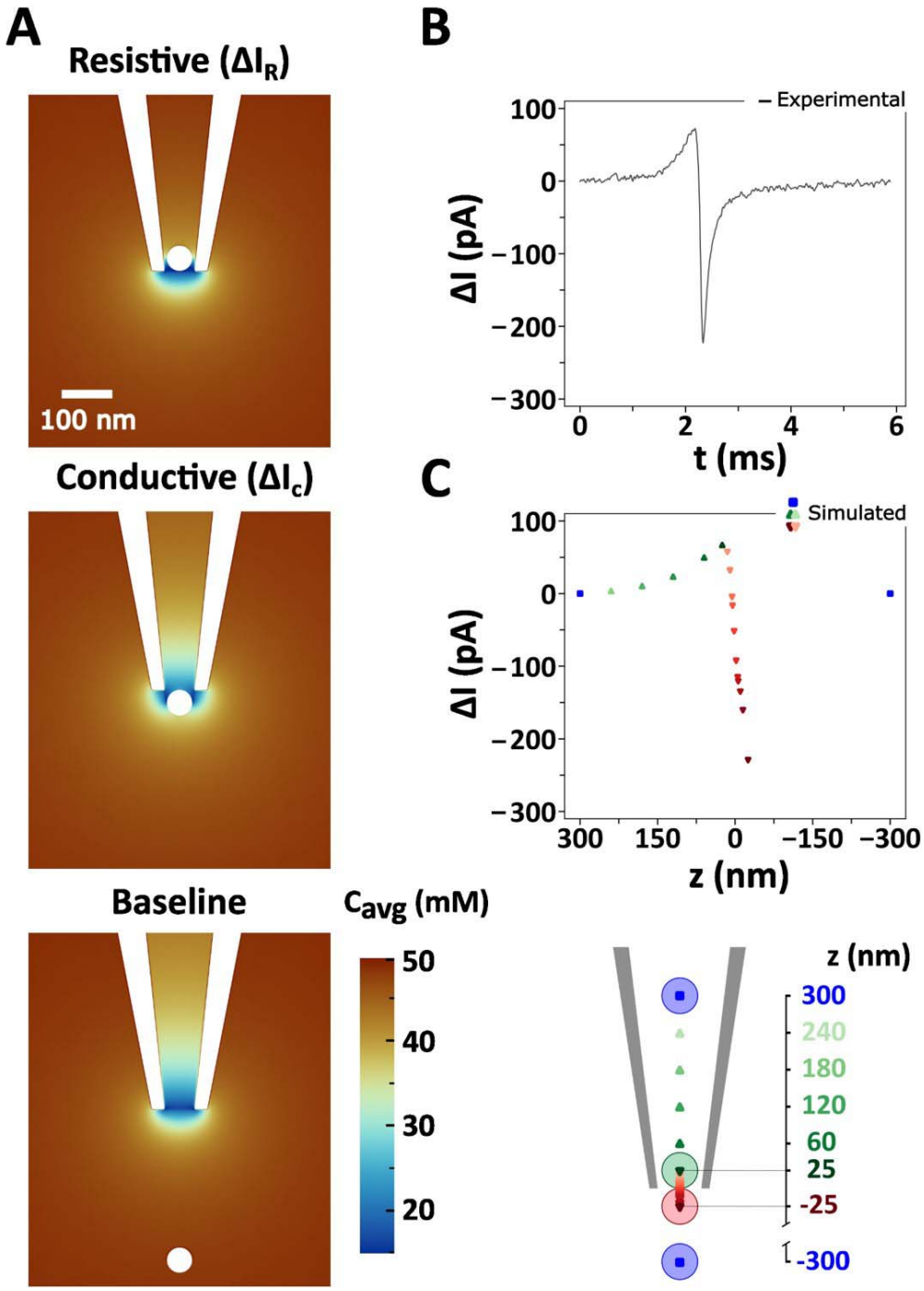

FIGURE 3. Finite element simulations of AuNP translocation. **(A)** Simulated ion distribution in the proximity of the nanopore tip utilizing a 50% PEG 50 mM KCl electrolyte bath with a 50 nm AuNP at different translocation positions through a 60 nm pore (left: inside the nanopore, middle: at the nanopore tip, right: outside in the bath). **(B)** Experimental (top panel) and simulated (middle panel) translocation signal of the 50 nm AuNP through a 60 nm pore with 50% PEG in 50 mM KCl electrolyte bath, and a nanopore schematic depicting the translocation distance used for simulated translocation signal (bottom panel).

Our polymer electrolyte system also enables the analysis of nanoparticles at low ionic strength (10 mM). Generally, nanopore measurements are carried out in high-salt conditions (> 100 mM KCl), excluding the analysis of less stable nanoparticles, such as bare citrate-capped nanoparticles (24). We probed the translocation of AuNPs and other citrate-capped nanoparticles diluted in 10mM KCl conditions, demonstrating that our nanopore measurements can reliably detect nanoparticle with high-capture rates and high signal-to-noise ratio (SNR), even in 10 mM KCl (Figure S11). Also, our approach enabled the analysis of bare silver and platinum citrate nanoparticles in 10 mM KCl (Figures S11B and S11C).

Inspired by the results above, we expanded our nanopore measurements to tackle complex anisotropic nanoparticles, such as branched gold nanostars (AuNS). We probed suspensions of AuNS with low and high degree of branching in 10 mM KCl following their different synthesis stages (Figure 4A). Similarly, we made use of a fixed nanopore size (80 nm) to probe the translocation of synthesized AuNS (Figure 4B), here named S5, S10, and S30, respectively, according to their degree of branching. The samples all exhibit a large amount of anisotropy which gives rise to their unique optical properties (Figure S13). With increasing branching density, we observed a broadening of the distributions both in terms of peak current amplitude and dwell time as shown in the scatter plots in Figure 3C. To evidence the progression in terms of nanopore detection from synthesis of AuNS (S5) to the high-density branched AuNS (S30) we computed a 95% confidence interval (CI) using the S5 translocation events as an input. We then applied this CI to the translocation events obtained for S10 AuNS and S30 AuNS samples. Based on this CI fitting we outlined an increase in the percentage (from the total number of events) of the events falling outside the S5 CI, namely 12% for the S10 and 35% for the S30 AuNS. Furthermore, we probed a

nanoparticle solution composed of S10 AuNS spiked with the 50 nm spherical uniform AuNPs. Their nominal hydrodynamic radius was broadly similar (60 nm vs 50 nm), but the ion current signals generated two clearly distinct populations indicating the potential of our approach for the quantitative analysis of anisotropic nanoparticles (Figure S12). In future, a more sophisticated analysis employing algorithmic models can reveal more subtle information concerning the ion current signals.

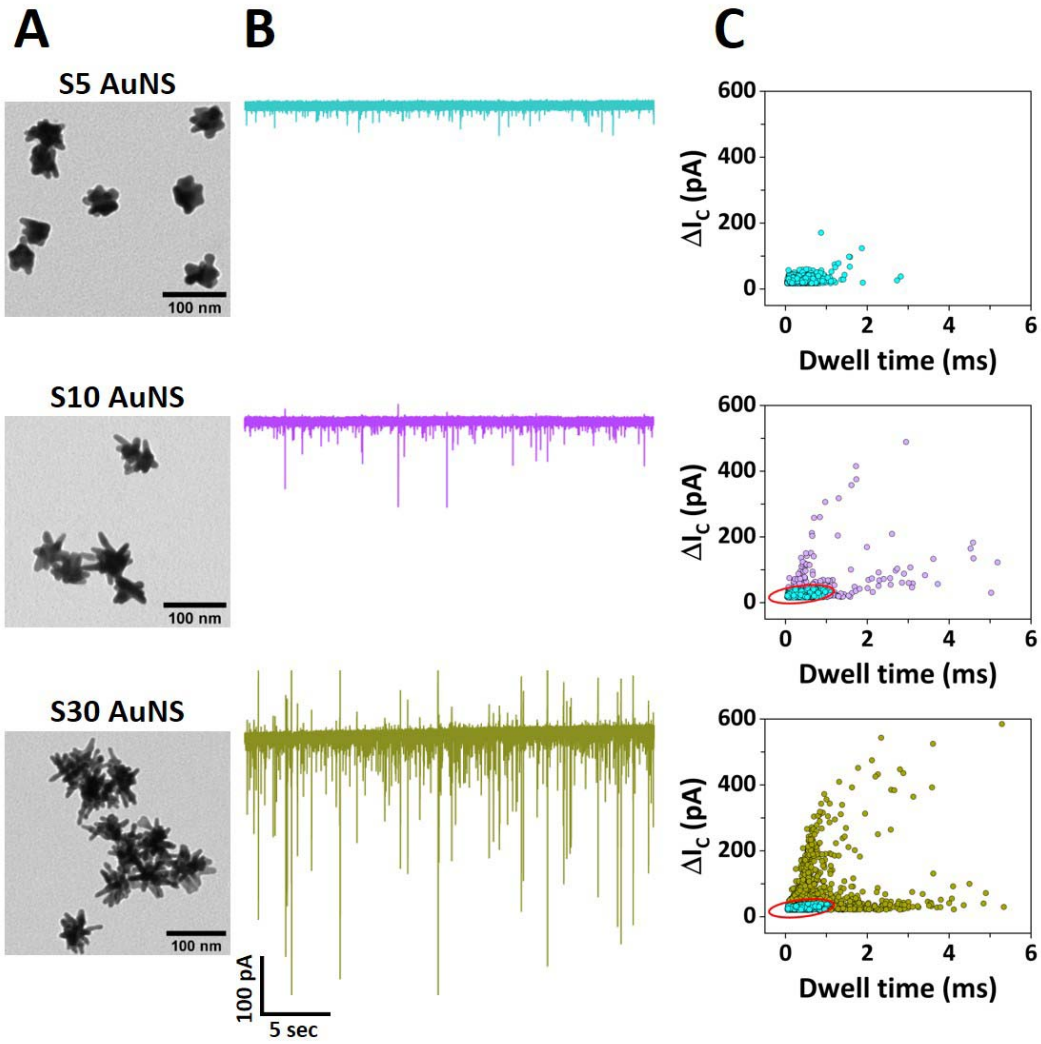

FIGURE 4. Nanopore sensing of synthesized AuNS. **(A)** TEM images of the S5 (top), S10 (middle), and S30 (bottom) synthesized AuNS (100 nm scale bar). **(B)** Current-time traces obtained for S5 (top), S10 (middle), and S30 (bottom) synthesized AuNS in 10 mM KCl 50% PEG conditions using a fixed pore size (80 nm) **(C)** Scatter plots of conductive peak currents as a function of dwell time for the S5 AuNS sample (top), S10 AuNS sample (middle), and S30 AuNS sample (bottom). The red

ellipse in the S10 and S30 scatter plot data indicates the 95% confidence interval of the S5 translocation events.

To further expand on the applicability of our polymer electrolyte enhanced nanopore system for investigating various functional nanostructures, we analysed the translocation of nanometre-sized proteins and protein spherical nucleic acids (ProSNAs). ProSNAs are a new class of "soft" nanoparticles with wide-spread applications in bottom-up materials assembly, intracellular sensing, and CRISPR-based gene editing (25-27). ProSNAs are based on the spherical nucleic acid (SNA) architecture and consist of a protein core functionalized with a dense shell of DNA strands (25). Compared to its analogous native protein, ProSNAs, *i.e.* the protein functionalized with ssDNA (single-stranded DNA), show an increase in cellular uptake, with the oligonucleotide density playing a critical role in the cellular uptake efficiency (27). Here, we used β-galactosidase (β-gal) ProSNAs thanks to their well-established stability and ease of synthesis (Figure S16 and S17). As depicted in Figure 5A, our polymer electrolyte enhanced sensing approach enabled the detection of the native β-gal protein and β-gal SNAs with two different DNA loadings: 22 ssDNAs (β-gal SNA_{22}) and 42 ssDNAs (β-gal SNA_{42}), respectively. The average conductive peak current obtained for the native β-gal protein was centred at 32 pA, whilst a ~3X increase for the β-gal SNA_{22} with a peak centred at 94 pA, and ~6X increase for the β -gal SNA_{42} was observed. Similarly, the dwell time between the native β-gal and the β-gal SNA_{22}, and between native β-gal and β-gal SNA42, increased by a factor of two and a factor of three, respectively. Apart from the discrimination between the native β-gal and the DNA functionalized β-gal SNAs, we were able to differentiate the β-gal SNAs with two different DNA loadings, evidenced by a clear increase in both in peak current amplitude and dwell time for their translocation under similar conditions (Figure 5B-C). Taken together, these results show that the polymer-

electrolyte nanopore system can enable the characterization of soft nanomaterials and allow for the discrimination of nanoparticles based on their functionalization state.

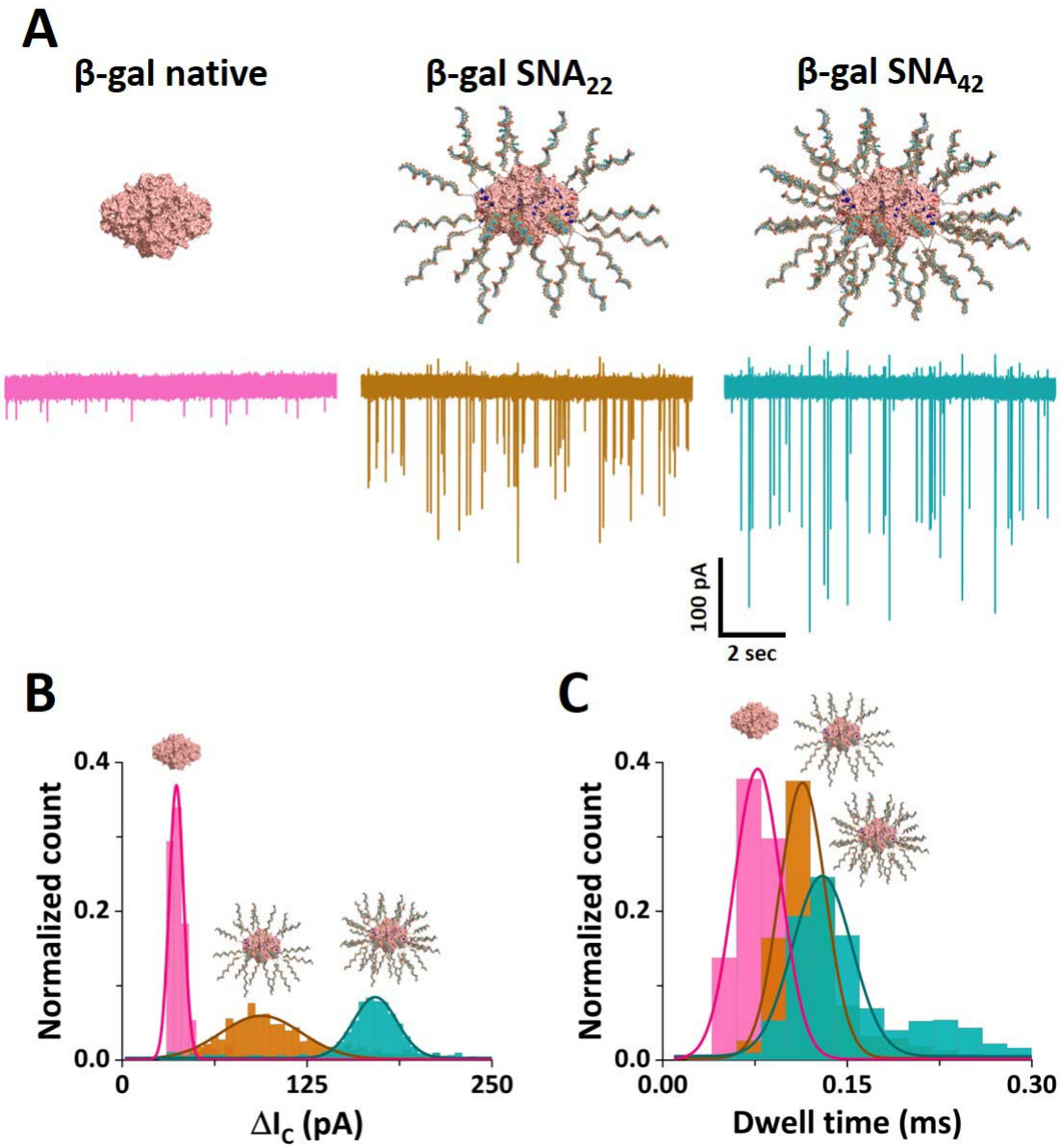

FIGURE 5 Nanopore sensing of protein spherical nucleic acids **(A)** Nanopore translocation ion current traces obtained with a fixed pore for the native β-gal (left), β-gal SNA_{22} (middle), and β-gal SNA_{42} (right). **(B)** Histograms of the conductive peak current for native β-gal (pink bars), β-gal SNA_{22} (brown bars), and β-gal SNA_{42} (teal bars). **(C)** Histograms of the dwell time for β-gal native (pink bars), β-gal SNA_{22} (brown bars), and β-gal SNA_{42} (teal bars).

CONCLUSIONS

We have demonstrated the development and implementation of a nanopore system enhanced by a polymer electrolyte enabling the analytical characterization of nanoparticles. Using experiments and finite element modelling. we provided a mechanistic description of the ion current signals and further employed the system to analyse heterogenous gold nanoparticle mixtures. We then demonstrated the unique ability of our approach to fingerprint nanoparticle samples at low ionic strength (10 mM) and exemplify the power of the system by characterizing the degree of branching of "hard" anisotropic Au nanostars and the nucleic acid coverage of "soft" proSNAs. This system will complement the toolbox of nanomaterials characterization technique and enable the real-time optimization of flow synthesis of a wide range of nanomaterials.

EXPERIMENTAL SECTION

Chemicals and materials. All reagents used in the translocation experiments were prepared using ultra-pure water (18.2 MΩ.cm) from Millipore system and further filtered through a 0.22µm syringe. KCl, Triton-X, EDTA, and PEG reagents were purchased from Sigma Aldrich. Gold PEG carboxyl-capped nanospheres (10, 20, 30, 40, and 50 nm diameter), silver citrate-capped nanospheres (30 nm diameter), and platinum citrate-capped nanospheres (30 nm nanospheres) were purchased from NanoComposix. Silver wire electrodes (0.25 mm diameter) used in the nanopore experiments were obtained from Alfa Aesar.

Standard nanoparticles characterization. The stability of the gold nanoparticles diluted in the KCl translocation buffer was probed by UV-Vis measurements (Figure S2) using a

NanoDrop ND-1000 spectrophotometer (Thermo Scientific). The size distribution of the standard nanoparticles in solution was determined by Zetasizer NanoZS (Malvern Instruments Ltd.) (Figure S3). All standard nanoparticle samples were used as received.

Nanopore fabrication and characterization. The nanopores were fabricated starting from 1.0 mm x 0.5 mm quartz capillaries (QF120-90-10; Sutter Instrument, UK) with the SU-P2000 laser puller (World Precision Instruments, UK), using a two-line program: (1) HEAT, 750; FILAMENT, 4, VELOCITY, 30; DELAY, 145, PULL, 80; (2) HEAT, 600, FILAMENT, 3; VELOCITY, 40; DELAY, 135; PULL, 150. The pulling parameters are instrument specific and lead to nanopipettes with a nanopore diameter of approximately 60 nm. The nanopipettes were characterized by measuring their pore resistance in 0.1 M KCl and the nanopore dimensions were confirmed by Scanning Electron Microscopy (SEM) using a Nova NanoSEM at an accelerating voltage of 3–5 kV (Figure S1).

Nanopore translocation measurements. Unless otherwise specified, the translocation experiments were carried out by filling the nanopipette with the translocation buffer (50 mM KCl, 0.01% Triton-X, 10 mM Tris, 1 mM EDTA, pH 8.0) containing the nanoparticles. The nanopipette was then immersed in a similar buffer with the addition of 50% (w/v) Polyethylene Glycol (PEG) 35 kDa (ultrapure grade, Sigma Aldrich). An Ag/AgCl wire (0.25 mm diameter, GoodFellow UK) was inserted in the nanopipette barrel and acted as the working electrode, while a second Ag/AgCl wire was immersed in the bath and acted as the counter and reference electrodes. The nanoparticles were driven from inside the nanopipette into the external bath by applying a negative potential to the working electrode placed inside the nanopipette with respect to the reference electrode in the bath. The ion current was recorded with a MultiClamp 700B patch-clamp amplifier (Molecular Devices) in voltage-clamp mode. Data was acquired at a 100 kHz sampling rate with a 20 kHz low-pass

filter using the pClamp10 software (Molecular Devices). The ion current traces were further analyzed with the MATLAB script Transanalyser, developed by Plesa *et al.(28).* The obtained translocation events were analysed by applying a 7-sigma threshold level from the baseline, and only the events above the threshold were considered as translocation events (S5). The obtained events were further analyzed and plotted using Origin 2019b.

Numerical simulations. To provide a mechanistic understanding of the experimentally observed current responses during nanoparticle translocation in our system, we developed numerical simulations describing the electric potential, ion concentrations, and fluid flow within and around the aperture of the glass nanopore. The simulations, which we describe briefly below, are based on a model we developed previously to describe a glass nanopore immersed in a polymer electrolyte (23). For a more detailed description, including a full list of parameters and boundary conditions, see the Supporting Information, section S18 (23). The commercial finite element software COMSOL Multiphysics (version 5.6) was used to solve the equations describing the spatially varying quantities listed above. Boundary conditions were selected to reflect the experimental system, including the surface charge on the glass/nanoparticle and the bulk solution concentrations. K+ and Cl- transport depends on the phase (PEG+KCl or KCl) with diffusion coefficients chosen to match the experimentally measured solution conductivities. In KCl, the diffusion coefficients of the K+ and Cl- are approximately equal (29) (DK+:DCl- = 0.49:0.51) while in the PEG DK+:DCl- = 0.35:0.65 ratio, as previously determined (23). The latter reflects cation affinity to PEG. For simplicity, the interface between the PEG+KCl and KCl was taken to have zero width, i.e., mixing of the solutions was neglected. In the absence of a nanoparticle, the interface was taken to be the disk exactly at the mouth of the pipette, while a nanoparticle translocation

was taken to perturb this interface outward (see Figure S18). The current was calculated from integrating the ion flux at the top of the nanopore.

Gold nanostars synthesis. First, citrate-capped gold nanoparticle (12 nm) seeds were synthesized using the Turkevich method (30). Briefly, 100 mL DI H2O boiling water and 200 µL of 0.5 M HAuCl4 were dispersed for 10 s. 15 mL of 1% trisodium citrate was added. After the final colour change, the solution was boiled for 15–30 min. Then the solution was cooled, filtered through a 0.22 µm nitrocellulose membrane, and stored at 4 °C until further use. The Au nanostars synthesis followed the Vo-Dinh group surfactant-free procedure with a few modifications (31). In brief, under room temperature and fast stirring, 10 mL of DI H2O, 10 µL 1 N HCl, and 493 µL of 0.5 M HAuCl4 were added to a plastic scintillation vial. Then, 100 µL of Au seeds were added, and 10 s afterward quickly added AgNO3 of various concentrations (1–3 mM; samples named S5, S10, and S30 relating to the AgNO3 final concentration, 5 µM, 10 µM, and 30 µM, respectively) and 50 µL of 0.1 M AA, simultaneously. Finally, 10 s afterward, transferred the stirred NS solution and immediately used. After the Au nanostar synthesis, 325 uL of thiol stabilizer (HS-PEG-COOH) was added to the Au nanostars, vortexed, then idle for 30 min at r.t. After 30 min., the solution was centrifuged and washed 3 times with DI H2O (1500 xg, 15 min, 4°C). Lastly, the samples were redispersed in DI H2O and stored at 4°C until used.

Gold nanostars characterization. Au Nanostars with thiol stabilizer were prepared for imaging by dropping 10 µL of 2-fold diluted sample onto a 200-mesh grid. The sample was allowed to dry overnight at room temperature. Then transmission electron microscope (TEM; Hitachi H7650) imaging was performed at 80 kV with an AMT BIOSPR16 camera. The TEM was available at Cincinnati Children's Hospital, the Pathology Research Core. To determine the size and concentration were measured via NanoSight NS300 nanoparticle

tracking analysis (NTA) system with a 532 nm laser. 20-, 40-, and 80-fold dilutions of the samples were used for the measurements. Extinction spectra of the samples were collected via a Biotek Microplate reader.

DNA synthesis and characterization. All oligonucleotides used in this work (Table S2) were synthesized using a MerMade 6 instrument (LGC, Biosearch Technologies) at 1 µmol scale. Reagents for DNA synthesis were purchased from Glen Research. Controlled pore glass (CPG) beads (Glen Research, Cat. No. 20-5041-10) were used as the solid-support for DNA synthesis. The synthesized products were cleaved from the CPG beads and deprotected using 0.5 mL of 30 % ammonium hydroxide (Thermo Fisher, Cat. No. A669) for 16 h at RT. After 16 h, the solution was run through a NAP™-5 column (Cytiva illustra™, Cat. No. 17085301) following manufacturer's protocol. The eluate was purified using reversed phase HPLC (Vanquish™ HPLC, Thermo Fisher, USA) using a C18 column (Thermo Fisher, Cat. No. 41005-259070A). A gradient of 0 to 70 % A→B over 40 min was used. A was 30 mM triethylammonium acetate (Thermo Fisher, Cat. No. O4885-1) with 3% (v/v) acetonitrile (Thermo Fisher, Cat. No. A996SK-4) and B was 100% acetonitrile. The collected fractions were lyophilized and redissolved in water. The mass of the oligonucleotides was determined using matrix-assisted laser desorption ionization time-of-flight mass spectrometry (MALDI-TOF MS, Bruker, AutoFlex Max) using 2',6'-dihydroxyacetophenone (DHAP, Sigma, Cat. No. 37468) as a matrix. The absorbance (A_λ) of oligonucleotides was measured as a function of wavelength (λ) using UV-Vis spectroscopy (Agilent, Cary 60 UV-Vis Spectrophotometer) using a quartz cuvette (Thermo Fisher, Cat. No. 50-753-2877) with 1 cm pathlength. Using the extinction coefficient (ε_λ) at 260 nm (obtained from the IDT Oligo Analyzer tool), the concentration (c) of the purified products was determined using Beer's law (Equation 1):

$$A_\lambda = \varepsilon_\lambda c l;\ l = 1\ cm \quad (1)$$

β-gal SNAs synthesis. β-gal ProSNAs were synthesized by following previously established procedures with some modifications (Figure S15) (25,26).A stock solution of β-Gal (Sigma, Cat. No. 10105031001) was exchanged into DPBS (Sigma, Cat. No. D8537) through centrifuge filtration (15000 rpm, 3 min, 4 °C, three times washing using a centrifuge (Thermo Fisher, Cat. No. 5425) using 100 kDa MWCO Amicon® filters (Thermo Fisher, Cat. No. UFC510096). The β-gal was then treated with TCEP (4 nM final concentration) and vortexed. Thereafter, the solution was passed through a NAP™-5 column to remove the TCEP and the purified β-gal solution was concentrated using a 100 kDa MWCO Amicon® filter. The protein concentration was determined via UV-vis spectroscopy using the extinction coefficient at the characteristic protein peak at 280 nm. Then 30-fold molar excess of Alexa Fluor™ 647 C_2 Maleimide (AF-647, Thermo Fisher, Invitrogen™, Cat. No. A20347) was added to the protein and the mixture was shaken overnight (1000 rpm, 4 °C) using a Benchmark MultiTherm Heating and Cooling Shaker (Marshall Scientific, Cat. No. H5000-HC). The solution was then rinsed multiple times with 0.1 M $NaHCO_3$ (Thermo Fisher, Cat. No. BP328-500) using a 100 kDa MWCO Amicon® filter to remove any unreacted dye. The absorbance of the filtrate was monitored at 650 nm to track the free dye. The washing was stopped when the absorbance at 650 nm was negligible. Using UV-vis spectroscopy, the concentration of the protein ($c_{\beta-gal}$) and the number of dyes attached per protein (N_{dye}) were calculated using Equations 2 and 3 below:

$$c_{\beta-gal} = \frac{A_{280\,nm} - \varepsilon_{280\,nm}^{AF-647} c_{AF-647}}{\varepsilon_{280\,nm}^{\beta-Gal}} \quad (2)$$

$$N_{dye} = \frac{c_{AF-647}}{c_{\beta-gal}} \quad (3)$$

c_{AF-647} is first determined using Equation 1, where $\varepsilon_{650\,nm}^{AF-647}$ = 270,000 M^{-1} cm^{-1}. The value for $\varepsilon_{280\,nm}^{AF-647}$ is 8,100 M^{-1} cm^{-1}.

Thereafter, NHS-PEG$_4$-azide (Thermo Scientific™, Cat. No. PI26130) was added to the dye-labeled β-gal (β-gal-AF) at 1000-fold molar excess and the reaction was incubated for 1.5 hours with shaking (1000 rpm, RT). The reaction mixture was then run through a NAP™-25 column (Cytiva illustra™, Cat. No. 17085202) and washed 5 times using centrifuge filtration (100 kDa MWCO Amicon® filters, 15000 rpm, 4 °C, 3 min per wash) to separate any free azide molecules. The protein concentration of the product (β-gal-AF-azide) was again determined via UV-vis spectroscopy. Then 50-fold molar excess of DBCO-DNA was added to β-gal-AF-azide (samples were prepared with both DBCO-DNA 1 and DBCO-DNA 2). The reaction was shaken for 3 days (1000 rpm, RT), following which the reaction mixture was washed several times using PBS and 100 kDa MWCO Amicon® filters (15000 rpm, 4 °C, 6 min per wash) to remove free DNA. The final product (β-gal SNAs) was characterized by UV-vis spectroscopy. First, based on the absorbance at 647 nm, c_{AF-647} was first determined. Then, using Equation 3, $c_{\beta-gal}$ was determined. Then, using the absorbance at 260 nm, the number of DNA per protein (N_{DNA}) was determined using Equation 4:

$$N_{DNA} = \frac{A_{260\,nm} - \varepsilon_{260\,nm}^{\beta-Gal}\, c_{\beta-gal}}{\varepsilon_{260\,nm}^{DNA} c_{\beta-gal}} \quad (4)$$

Based on these calculations, we determined that the final β-gal SNAs had an average of ~2 dyes and ~42 DNA strands on the protein surface for DBCO-DNA 1 and ~5 dyes and ~22 DNA strands on the protein surface for DBCO-DNA 2.

β-gal SNAs characterization. The synthesis of β-gal SNAs was confirmed through native PAGE gel electrophoresis and UV-Vis. For the PAGE gel electrophoresis, 10 µL of 1 µM SNAs (by protein) was added to 2 µL of glycerol and loaded onto a 4-15% acrylamide gel (Bio-Rad, 4-15% Mini-PROTEAN® TGX™ Precast Protein Gels, 10-well, Cat. No. 4561084) and run for 60 min at 100V at room temperature. The running buffer was prepared by diluting 10X Tris-Borate-EDTA (TBE Buffer, Thermo Fisher, Cat. No. BP13334) to obtain a 1X TBE Buffer. The native protein was also run as a control. 5 µL EZ-Run Prestained Rec Protein Ladder (Thermo Fisher, Cat. No. BP3603500) was also used. For β-gal, after electrophoresis, a solution of 10 mM ortho-nitrophenyl-β-D-galactopyranoside (ONPG, Sigma, Cat. No. N1127) the protein substrate was added to the gel to identify the positions of active proteins. Thereafter, the gels were stained with GelRed® Nucleic Acid Gel Stain following the manufacturer's protocol and imaged using the ChemiDoc™ MP Imaging System (Bio-Rad, USA). Subsequently, the gels were stained with SimplyBlue SafeStain (Thermo Fisher, Cat. No. LC6065) following the manufacturer's protocol and reimaged. The number of dyes and DNA strands per protein were calculated using the absorbance spectra, as shown Figure S17.

Declaration of Interests. The authors declare no competing interests.

Acknowledgements.

The authors gratefully acknowledge Dr. Zabeada Aslam and the Leeds Electron Microscopy and Spectroscopy centre (LEMAS) for their support and assistance with TEM characterization of the gold nanoparticles. We thank Dr. Alexander Kulak for the help provided with SEM imaging of the nanopipettes. S.C. and P.A. acknowledge funding from the European Union's Horizon 2020 research and innovation 7 program under the Marie Skłodowska-Curie MSCA-ITN grant agreement no. 812398, through the single-entity nanoelectrochemistry, SENTINEL, project. P.A. Acknowledge funding from the European

Research Council (ERC) under the project DYNAMIN, grant agreement no. 788968. G.M. acknowledges funding from a University of Leeds Scholarship. P.A and C.W. acknowledge funding from the Engineering and Physical Sciences Research Council UK (EPSRC) Healthcare Technologies for the grant EP/W004933/1, and C.W. acknowledges funding from the Medical Research Council (MRC) UK under the grant number MR/N029976/1. Schematics used in our figures were adapted from BioRender.com.

REFERENCES

1. Zhang, H. 2020. Molecularly Imprinted Nanoparticles for Biomedical Applications. *Advanced Materials*. 32(3):1806328, doi: https://doi.org/10.1002/adma.201806328.
2. Tan, H. W., J. An, C. K. Chua, and T. Tran. 2019. Metallic Nanoparticle Inks for 3D Printing of Electronics. *Advanced Electronic Materials*. 5(5):1800831, doi: https://doi.org/10.1002/aelm.201800831.
3. Wang, L., M. Hasanzadeh Kafshgari, and M. Meunier. 2020. Optical Properties and Applications of Plasmonic-Metal Nanoparticles. *Advanced Functional Materials*. 30(51):2005400, doi: https://doi.org/10.1002/adfm.202005400.
4. Xu, X., D. Valavanis, P. Ciocci, S. Confederat, F. Marcuccio, J.-F. Lemineur, P. Actis, F. Kanoufi, and P. R. Unwin. 2023. The New Era of High-Throughput Nanoelectrochemistry. *Analytical Chemistry*. 95(1):319-356, doi: 10.1021/acs.analchem.2c05105.
5. Tomaszewska, E., K. Soliwoda, K. Kadziola, B. Tkacz-Szczesna, G. Celichowski, M. Cichomski, W. Szmaja, and J. Grobelny. 2013. Detection limits of DLS and UV-Vis spectroscopy in characterization of polydisperse nanoparticles colloids. *Journal of Nanomaterials*. 2013:60-60
6. Modena, M. M., B. Rühle, T. P. Burg, and S. Wuttke. 2019. Nanoparticle Characterization: What to Measure? *Advanced Materials*. 31(32):1901556, doi: https://doi.org/10.1002/adma.201901556.
7. Lee, K., K.-B. Park, H.-J. Kim, J.-S. Yu, H. Chae, H.-M. Kim, and K.-B. Kim. 2018. Recent Progress in Solid-State Nanopores. *Advanced Materials*. 30(42):1704680, doi: https://doi.org/10.1002/adma.201704680.
8. Yang, W., B. Radha, A. Choudhary, Y. You, G. Mettela, A. K. Geim, A. Aksimentiev, A. Keerthi, and C. Dekker. 2021. Translocation of DNA through Ultrathin Nanoslits. *Advanced Materials*. 33(11):2007682, doi: https://doi.org/10.1002/adma.202007682.
9. Ren, R., M. Sun, P. Goel, S. Cai, N. A. Kotov, H. Kuang, C. Xu, A. P. Ivanov, and J. B. Edel. 2021. Single-Molecule Binding Assay Using Nanopores and Dimeric NP Conjugates. *Advanced Materials*. 33(38):2103067, doi: https://doi.org/10.1002/adma.202103067.
10. German, S. R., L. Luo, H. S. White, and T. L. Mega. 2013. Controlling Nanoparticle Dynamics in Conical Nanopores. *The Journal of Physical Chemistry C*. 117(1):703-711, doi: 10.1021/jp310513v.

11. Smeets, R. M. M., U. F. Keyser, D. Krapf, M.-Y. Wu, N. H. Dekker, and C. Dekker. 2006. Salt Dependence of Ion Transport and DNA Translocation through Solid-State Nanopores. *Nano Letters*. 6(1):89-95, doi: 10.1021/nl052107w.
12. Kowalczyk, S. W., D. B. Wells, A. Aksimentiev, and C. Dekker. 2012. Slowing down DNA Translocation through a Nanopore in Lithium Chloride. *Nano Letters*. 12(2):1038-1044, doi: 10.1021/nl204273h.
13. Platt, M., G. R. Willmott, and G. U. Lee. 2012. Resistive Pulse Sensing of Analyte-Induced Multicomponent Rod Aggregation Using Tunable Pores. *Small*. 8(15):2436-2444, doi: https://doi.org/10.1002/smll.201200058.
14. Maugi, R., P. Hauer, J. Bowen, E. Ashman, E. Hunsicker, and M. Platt. 2020. A methodology for characterising nanoparticle size and shape using nanopores. *Nanoscale*. 12(1):262-270, doi: 10.1039/C9NR09100A.
15. Chau, C., F. Marcuccio, D. Soulias, M. A. Edwards, A. Tuplin, S. E. Radford, E. Hewitt, and P. Actis. 2022. Probing RNA Conformations Using a Polymer–Electrolyte Solid-State Nanopore. *ACS Nano*. 16(12):20075-20085, doi: 10.1021/acsnano.2c08312.
16. Prabhu, A. S., T. Z. N. Jubery, K. J. Freedman, R. Mulero, P. Dutta, and M. J. Kim. 2010. Chemically modified solid state nanopores for high throughput nanoparticle separation. *Journal of Physics: Condensed Matter*. 22(45):454107, doi: 10.1088/0953-8984/22/45/454107.
17. Wen, C., S. Zeng, Z. Zhang, and S.-L. Zhang. 2018. Group Behavior of Nanoparticles Translocating Multiple Nanopores. *Analytical Chemistry*. 90(22):13483-13490, doi: 10.1021/acs.analchem.8b03408.
18. Lan, W.-J., D. A. Holden, B. Zhang, and H. S. White. 2011. Nanoparticle Transport in Conical-Shaped Nanopores. *Analytical Chemistry*. 83(10):3840-3847, doi: 10.1021/ac200312n.
19. Sensale, S., Z. Peng, and H.-C. Chang. 2019. Biphasic signals during nanopore translocation of DNA and nanoparticles due to strong ion cloud deformation. *Nanoscale*. 11(47):22772-22779, doi: 10.1039/C9NR05223B.
20. Chen, K., L. Shan, S. He, G. Hu, Y. Meng, and Y. Tian. 2015. Biphasic Resistive Pulses and Ion Concentration Modulation during Particle Translocation through Cylindrical Nanopores. *The Journal of Physical Chemistry C*. 119(15):8329-8335, doi: 10.1021/acs.jpcc.5b00047.
21. Menestrina, J., C. Yang, M. Schiel, I. Vlassiouk, and Z. S. Siwy. 2014. Charged Particles Modulate Local Ionic Concentrations and Cause Formation of Positive Peaks in Resistive-Pulse-Based Detection. *The Journal of Physical Chemistry C*. 118(5):2391-2398, doi: 10.1021/jp412135v.
22. Lastra, L. S., Y. M. N. D. Y. Bandara, M. Nguyen, N. Farajpour, and K. J. Freedman. 2022. On the origins of conductive pulse sensing inside a nanopore. *Nature Communications*. 13(1):2186, doi: 10.1038/s41467-022-29758-8.
23. Marcuccio, F., D. Soulias, C. C. C. Chau, S. E. Radford, E. Hewitt, P. Actis, and M. A. Edwards. 2023. Mechanistic Study of the Conductance and Enhanced Single-Molecule Detection in a Polymer–Electrolyte Nanopore. *ACS Nanoscience Au*. doi: 10.1021/acsnanoscienceau.2c00050.
24. Wei, X., A. Popov, and R. Hernandez. 2022. Electric Potential of Citrate-Capped Gold Nanoparticles Is Affected by Poly(allylamine hydrochloride) and Salt Concentration. *ACS Applied Materials & Interfaces*. 14(10):12538-12550, doi: 10.1021/acsami.1c24526.

25. Ebrahimi, S. B., D. Samanta, C. D. Kusmierz, and C. A. Mirkin. 2022. Protein transfection via spherical nucleic acids. *Nature Protocols*. 17(2):327-357, doi: 10.1038/s41596-021-00642-x.
26. Samanta, D., S. B. Ebrahimi, C. D. Kusmierz, H. F. Cheng, and C. A. Mirkin. 2020. Protein Spherical Nucleic Acids for Live-Cell Chemical Analysis. *Journal of the American Chemical Society*. 142(31):13350-13355, doi: 10.1021/jacs.0c06866.
27. Samanta, D., S. B. Ebrahimi, and C. A. Mirkin. 2020. Nucleic-Acid Structures as Intracellular Probes for Live Cells. *Advanced Materials*. 32(13):1901743, doi: https://doi.org/10.1002/adma.201901743.
28. Plesa, C., and C. Dekker. 2015. Data analysis methods for solid-state nanopores. *Nanotechnology*. 26(8):084003
29. Haynes, W. M. 2016. CRC handbook of chemistry and physics. CRC press.
30. Turkevich, J., P. C. Stevenson, and J. Hillier. 1951. A study of the nucleation and growth processes in the synthesis of colloidal gold. *Discussions of the Faraday Society*. 11:55-75
31. Yuan, H., C. G. Khoury, H. Hwang, C. M. Wilson, G. A. Grant, and T. Vo-Dinh. 2012. Gold nanostars: surfactant-free synthesis, 3D modelling, and two-photon photoluminescence imaging. *Nanotechnology*. 23(7):075102